


Microbiota-indole-3-propionic acid-heart axis mediates the protection of leflunomide against α PD1-induced cardiotoxicity in mice

Received: 17 May 2024

Accepted: 12 March 2025

Published online: 19 March 2025

Rong Huang^{1,2,4}, Zhuo-Yu Shen^{1,2,4}, Dan Huang^{1,2}, Shu-Hong Zhao^{1,2},
Ling-Xuan Dan^{1,2}, Pan Wu³, Qi-Zhu Tang^{1,2} & Zhen-Guo Ma^{1,2} 

Anti-programmed death 1 (α PD1) immune checkpoint blockade is used in combination for cancer treatment but associated with cardiovascular toxicity. Leflunomide (Lef) can suppress the growth of several tumor and mitigate cardiac remodeling in mice. However, the role of Lef in α PD1-induced cardiotoxicity remains unclear. Here, we report that Lef treatment inhibits α PD1-related cardiotoxicity without compromising the efficacy of α PD1-mediated immunotherapy. Lef changes community structure of gut microbiota in α PD1-treated melanoma-bearing mice. Moreover, mice receiving microbiota transplants from Lef+ α PD1-treated melanoma-bearing mice have better cardiac function compared to mice receiving transplants from α PD1-treated mice. Mechanistically, we analyze metabolomics and identify indole-3-propionic acid (IPA), which protects cardiac dysfunction in α PD1-treated mice. IPA can directly bind to the aryl hydrocarbon receptor and promote phosphoinositide 3-kinase expression, thus curtailing the cardiomyocyte response to immune injury. Our findings reveal that Lef mitigates α PD1-induced cardiac toxicity in melanoma-bearing mice through modulation of the microbiota-IPA-heart axis.

Melanoma represents around 5% of all skin cancer cases, with a 65% mortality rate, posing a grave threat to human health^{1,2}. Immune checkpoint inhibition is a long-established treatment, increasing the survival rate for ~40% of melanoma patients^{3,4}. Anti-programmed death 1 (α PD1), an immune checkpoint inhibitor, has achieved great clinical success in anti-melanoma therapy. α PD1 primarily targets immune checkpoints to reactivate dormant T cells, leading to melanoma cell death⁵. However, patients treated with α PD1 develop immune-related adverse events, of which cardiotoxicity is the most lethal^{6,7}. α PD1-associated cardiotoxicity is characterized by significant cardiovascular complications, including myocarditis, pericarditis, and cardiomyopathy. Cardiomyocyte necrosis and apoptosis are key pathological features of α PD1-associated cardiotoxicity⁸. Disruption of cardiac immune homeostasis and myocardial inflammation accumulation were closely involved in α PD1-related cardiotoxicity⁹. NACHT,

LRR, and PYD domains-containing protein 3 (NLRP3) inflammasome may be a key driver of α PD1-related cardiotoxicity and hyperglycemia may worsen the outcome of patients receiving α PD1 therapy^{10,11}. α PD1-induced intestinal barrier dysfunction and alterations in gut microbiota also had negative impacts on cardiac function^{12,13}. Recent research has advocated interventions to mitigate α PD1-related cardiotoxicity, emphasizing the cytotoxic impact of T cells on cardiomyocytes and the pro-inflammatory cytokines liberation⁷. However, focusing on inhibiting T cells and the pro-inflammatory cytokines may also dampen the anti-tumor effects of α PD1¹⁴. Therefore, it is imperative to explore pharmacological interventions that can effectively suppress α PD1-related cardiotoxicity but not compromise the efficacy of α PD1-mediated immunotherapy.

Leflunomide (Lef), currently used in clinical practice for treating rheumatoid arthritis, is an immunomodulatory drug¹⁵. Studies have

¹Department of Cardiology, Renmin Hospital of Wuhan University, Wuhan, PR China. ²Hubei Key Laboratory of Metabolic and Chronic Diseases, Wuhan, PR China. ³Department of Adult Internal Medicine, Maternal and Child Health Hospital of Hubei Province, Tongji Medical College, Huazhong University of Science and Technology, Wuhan, Hubei, PR China. ⁴These authors contributed equally: Rong Huang, Zhuo-Yu Shen. ✉e-mail: zhengma@whu.edu.cn

shown that Lef can hinder the growth of melanoma in mice by inhibiting dihydroorotate dehydrogenase (DHODH)¹⁶. Our previous research has also demonstrated that Lef can alleviate cardiac remodeling and reduce myocardial fibrosis in mice. Interestingly, the observed effects were not reliant on DHODH¹⁷. Therefore, we hypothesize that Lef could attenuate α PD1-induced cardiotoxicity in melanoma-bearing mice. In this study, the effect of Lef on α PD1-associated cardiotoxicity was investigated in melanoma mice. We then found that the protection of Lef in α PD1-induced cardiotoxicity was not dependent on CD8⁺ T cells. Mechanistically, our study revealed that the microbiota-indole-3-propionic acid (IPA)-cardiac aryl hydrocarbon receptor (AhR) axis was responsible for the cardioprotective effects of Lef by modulating the phosphoinositide 3-kinase (PI3K)-protein kinase B (AKT) pathway to prevent myocardial apoptosis in α PD1-treated melanoma mice. Our findings identify a specific mechanism of action for Lef in α PD1-associated cardiotoxicity and may provide a potential therapeutic target.

Results

Lef treatment enhanced the efficacy of α PD1-mediated immunotherapy against melanoma progression

To investigate the impact of Lef on the anti-tumor properties of PD1 inhibitors, B16-F10 cells were subcutaneously transplanted into the right abdomen of mice. Mice were intraperitoneally injected with α PD1 or IgG, and subjected to Lef treatment for 12 days (Fig. 1A). α PD1-treated mice showed a significant reduction in tumor size compared to the control mice. Mice treated with α PD1+Lef had notably smaller tumor volumes than those treated with α PD1 alone (Fig. 1B, C, Supplementary Fig. 1A). Lef did not prevent mice from losing body weight in response to α PD1 during the course of the experiment (Supplementary Fig. 1B). B16-F10 is usually a cold tumor, which might not respond to anti-PD1 therapy. Therefore, we evaluate the impact of Lef on an established melanoma model. Starting from 14 days post-tumor transplantation, mice received intraperitoneal injections of α PD1 every other day. At the first time of α PD1 injection, these mice received a daily treatment of Lef. We observed a similar therapeutic efficacy of Lef on melanoma volumes (Supplementary Fig. 1C, D). To observe the

survival rate of this established melanoma model, we extended the tumor inoculation time to 45 days. α PD1 therapy decreased melanoma mice death. The therapeutic effect of α PD1 in melanoma mice was enhanced by the use of Lef (Supplementary Fig. 1E). An increase in the number of CD4⁺ and CD8⁺ T cells was observed in α PD1 mice compared to the control group. Lef significantly decreased CD8⁺ T cells in the tumor tissues of α PD1 mice without affecting CD4⁺ T cells (Fig. 1D). We also used a flow cytometry gating strategy to count T cells in melanoma. We observed that Lef decreased CD8⁺ T cells in the tumor tissues of α PD1 mice (the ratio of CD8⁺ to CD45⁺ cells: α PD1+Veh, $6.98 \pm 0.29\%$; α PD1+Lef, $4.07 \pm 0.18\%$, $P < 0.05$) (Supplementary Fig. 1F–H). A previous study reported that Lef could hinder the growth of melanoma by inhibiting the transcriptional elongation of genes required for tumor growth¹⁶. As expected, we also found that Lef reduced tumor proliferation in α PD1-treated mice without affecting tumor death (Supplementary Fig. 1I, J). These findings indicate that α PD1 inhibits melanoma growth in mice and that Lef enhances the anti-tumor effect of α PD1.

Lef treatment attenuated cardiotoxicity in α PD1-treated melanoma mice

α PD1-treated melanoma mice exhibited an impaired cardiac function, as suggested by the decreased ejection fraction (EF) and fractional shortening (FS), and the increased left ventricular end-diastolic internal diameter (LVIDd). These pathological alterations were prevented by the treatment of Lef (Fig. 2A–D). There was no significant difference in heart rate (HR) among all four groups (Supplementary Fig. 1K). We also found that Lef treatment improved cardiac output (CO) in α PD1-treated melanoma mice (Supplementary Fig. 1L). Global longitudinal strain (GLS) is identified as a sensitive marker of cardiotoxicity in patients receiving standard chemotherapy¹⁸. To further evaluate the adverse effect of α PD1 injection, 2D speckle-tracking echocardiography and strain analysis were performed. Segmental assessment of left ventricular function using GLS and average radial strain (ARS) analysis revealed an increased GLS and ARS in the anterior segments of α PD1+Lef mice compared to those in α PD1 mice (Fig. 2E–G, Supplementary Fig. 2A, B). Additionally, α PD1 injection

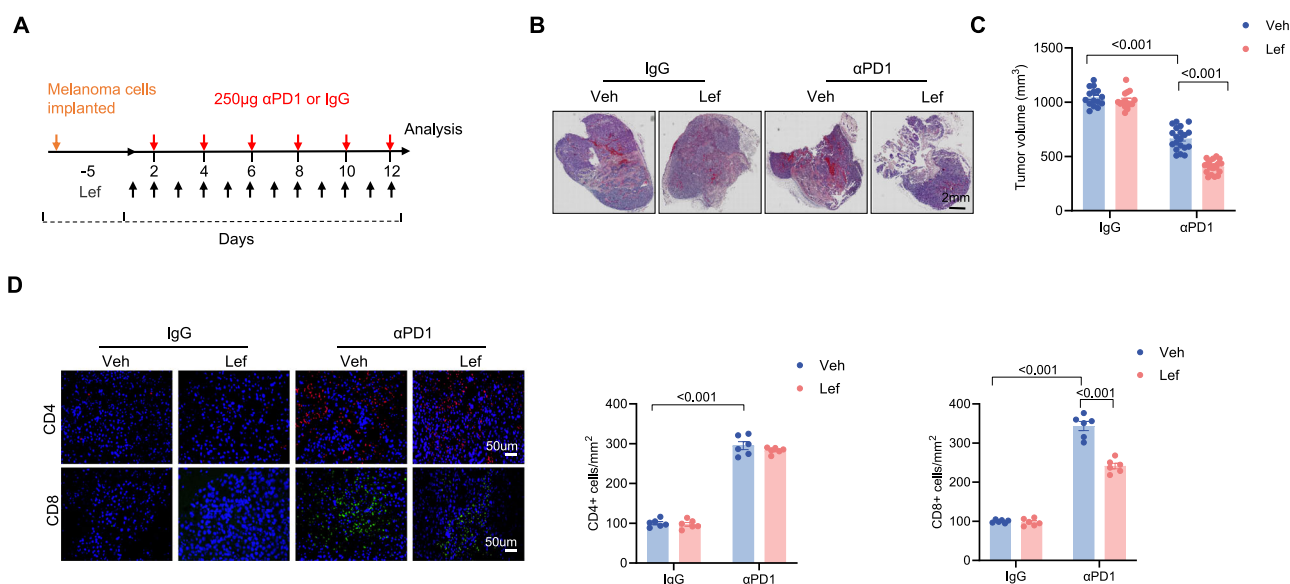


Fig. 1 | Lef enhanced the efficacy of α PD1-mediated immunotherapy against melanoma progression. **A** Schematic representation of the experimental design for establishing a model of PD1 inhibitors-related cardiotoxicity in mice, encompassing the administration schedule of both PD1 inhibitor (administered intraperitoneally at 250 μ g/kg on alternate days) and leflunomide (given daily at 10 mg/kg). **B** Hematoxylin and eosin (H&E) staining illustrates the histological features of

melanoma tumor sections. **C** Quantification reveals the temporal evolution of melanoma tumor volume across groups (IgG control, $n = 15$; α PD1-treated, $n = 20$). **D** Assessment of CD4⁺ (red) and CD8⁺ (green) T lymphocyte infiltration within tumor tissues from different groups ($n = 6$). Nuclei are stained with DAPI (blue). Data are shown as the mean \pm SEM and analyzed using one-way ANOVA with post hoc tests.

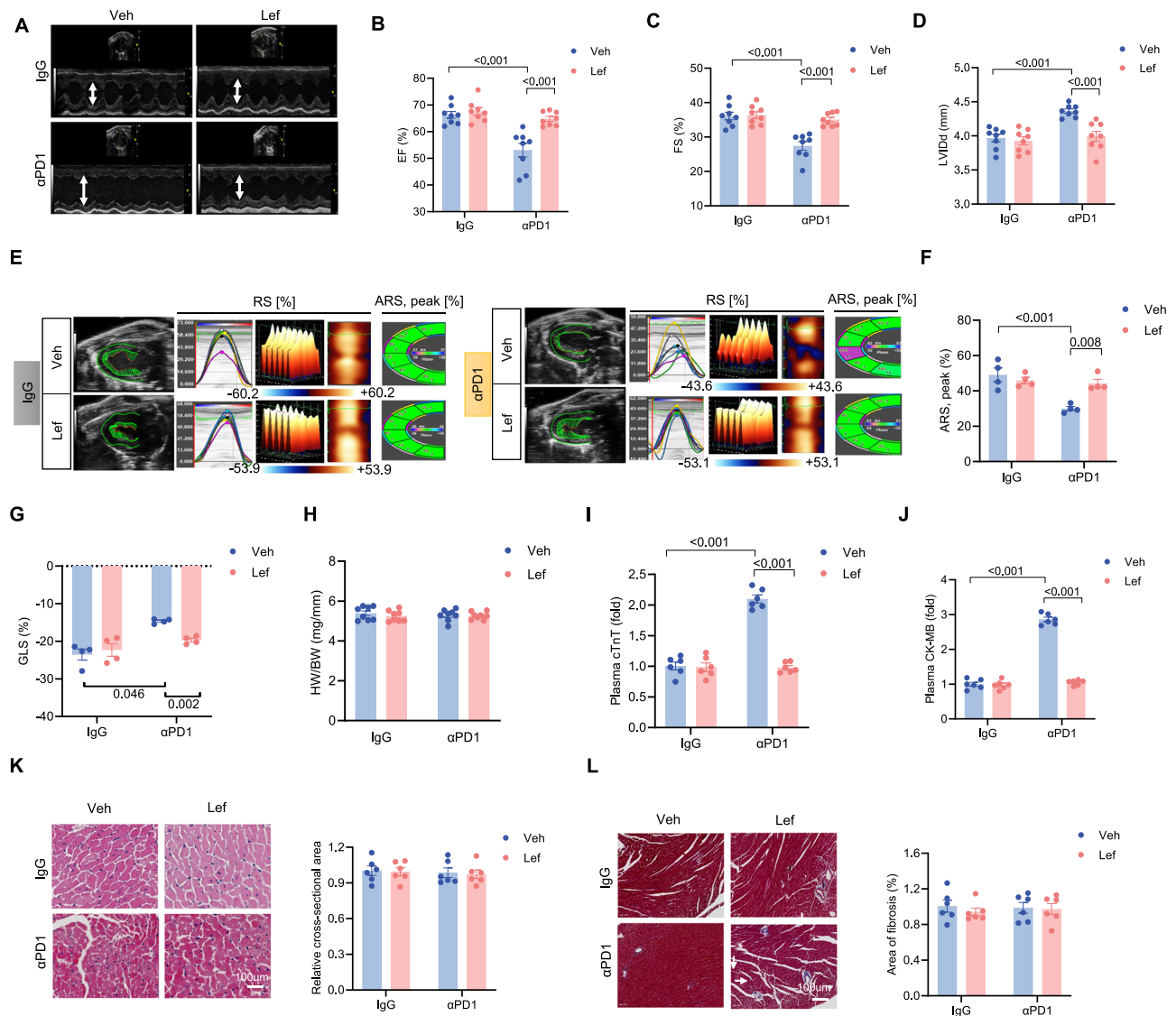


Fig. 2 | Lef attenuated cardiotoxicity in αPD1-treated melanoma mice.

A Representative M-mode echocardiographic images of the left ventricle. Ejection fraction (EF) (**B**) and Fractional shortening (FS) (**C**) and Left ventricular end-diastolic internal diameter (LVIDd) (**D**) were detected in these groups ($n = 8$). 2D speckle-tracking echocardiography and strain analysis (ARS) (**E**) and Average radial strain (ARS) (**F**) and Global longitudinal strain (GLS) (**G**) ($n = 4$). **H** Heart weight-to-body

weight ratio (HW/BW) ($n = 8$). **I, J** Plasma biomarker assessments revealing levels of cardiac troponin T (cTnT) and creatine kinase-MB (CK-MB) ($n = 6$). **K** HE staining and quantification of cardiomyocyte cross-sectional area ($n = 6$). **L** Masson trichrome staining and quantification of cardiac fibrosis ($n = 6$). Data are shown as the mean \pm SEM and analyzed using one-way ANOVA with post hoc tests.

resulted in regional contractile dysfunction, as suggested by reductions in average radial displacement and velocity measurements in αPD1-treated mice, and this pathological effect was largely attenuated after Lef treatment (Fig. 2E–G, Supplementary Fig. 2A, B). There was no significant difference in heart weight/body weight among all four groups (Fig. 2H). αPD1 injection resulted in severe cardiac injury, as indicated by the elevated cardiac troponin T (cTnT) and creatine kinase-MB (CK-MB). These adverse effects were attenuated in melanoma mice treated with Lef (Fig. 2I, J). Unexpectedly, HE staining and Masson's trichrome staining showed no significant difference in the cross-sectional area of cardiomyocytes and cardiac fibrosis among all four groups (Fig. 2K, L).

To further investigate the effect of Lef in attenuating αPD1-induced cardiotoxicity, RNA sequencing was performed on the hearts, revealing alterations in 2490 genes related to αPD1 vs αPD1+Lef under the conditions of fold change >2 and adjusted P value <0.05 . Of these genes, 1548 were upregulated and 942 were downregulated (Fig. 3A).

KEGG term analysis of differentially expressed genes (DEGs) revealed that several signaling pathways were closely related to tissue protection against injury, specifically PI3K-AKT signaling pathway, cytokine-cytokine receptor interaction and focal adhesion (Fig. 3B). Patchy inflammatory infiltrates and cardiomyocyte death are the most definitive means of αPD1-induced cardiotoxicity¹⁹. Lef treatment resulted in minimal effects on myocardial inflammation of melanoma mice after αPD1 injection (Supplementary Fig. 3A). Immunofluorescence staining demonstrated that Lef decreased cardiac CD8+ T cell infiltration in αPD1-treated melanoma mice without affecting CD4+ T cell infiltration (Fig. 3C, Supplementary Fig. 3B). Consistent with our expectations, Lef reduced Bax expression and increased Bcl2 expression upon αPD1 stimulation (Fig. 3D). αPD1 increased apoptosis in the heart, which was significantly inhibited by Lef treatment (Fig. 3E). Hence, our findings suggested that Lef attenuated cardiac myocyte death and CD8+ T cell infiltration in αPD1-treated melanoma mice, signifying the importance of Lef in this disease.

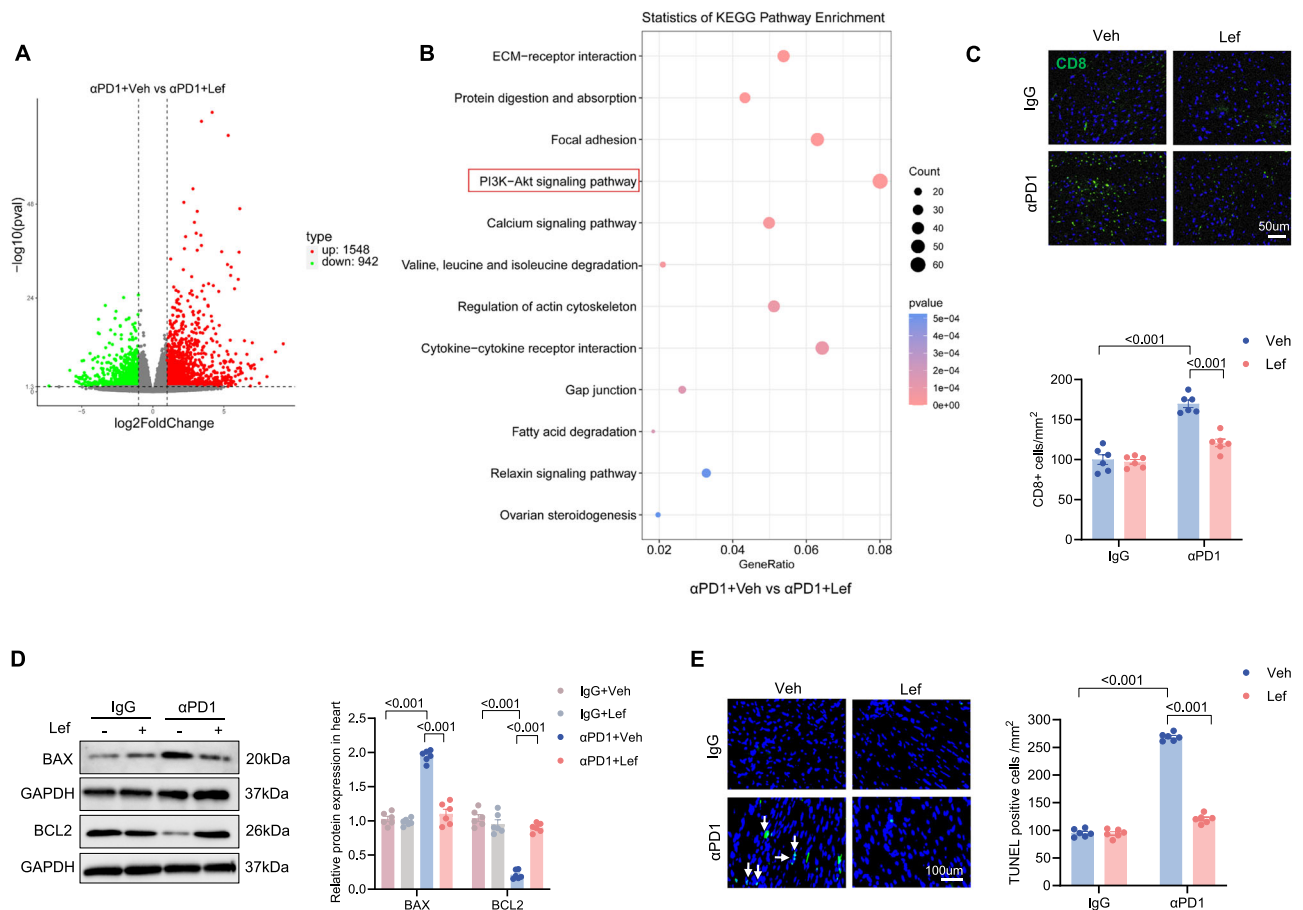


Fig. 3 | Lef effectively suppresses PD1 inhibitor-induced apoptosis in mice cardiomyocytes. **A** Volcano plots of the upregulated genes (red) and down-regulated genes (green) of α PD1 and α PD1+Lef groups ($n = 4$). The differential expression of genes (DEGs) between the two groups was analyzed using the DESeq2 R package (two-sided). **B** The analysis depicts the enriched Kyoto Encyclopedia of Genes and Genomes (KEGG) pathways among genes showing altered expression in melanoma-bearing mice treated with either α PD1+Veh or α PD1+Lef (two-sided).

C Immunofluorescent staining for cardiac CD8+ T cells (green) in various treatment groups, highlighting their distribution and infiltration ($n = 6$). Nuclei are stained with DAPI (blue). **D** Representative western blots of BAX and BCL2 protein expression in hearts ($n = 6$). **E** Terminal deoxynucleotidyl transferase dUTP Nick End Labeling (TUNEL) staining and apoptosis rate in cardiac tissues (green, arrows indicate positive signals) ($n = 6$). Nuclei are stained with DAPI (blue). Data are shown as the mean \pm SEM and analyzed using one-way ANOVA with post hoc tests.

Cardioprotective effects of Lef in α PD1 mice are not dependent on T cells

To investigate whether CD8+ T cells were responsible for the cardioprotective effects of Lef in α PD1 mice, we conducted a depletion study using a CD8 monoclonal antibody. Melanoma mice treated with α PD1 were intraperitoneally given α CD8 every other day (Supplementary Fig. 4A). The success of the experiment was confirmed by examining CD8-positive cells via immunofluorescence, showing effective depletion of CD8+ T cells in the hearts (Supplementary Fig. 4B). Lef supplementation also alleviated cardiac injury and cardiac dysfunction in α PD1-treated melanoma mice following CD8+ T cell depletion, as indicated by EF, FS, B-type natriuretic peptide (BNP) mRNA level and cTnT concentration (Supplementary Fig. 4C–F). Next, we evaluated whether Lef supplementation could provide a direct effect on adult cardiomyocytes isolated from α PD1-treated melanoma mice. Lef is almost completely metabolized (>95%) to its active compound A77 1726 after administration, which causes the main effects of Lef²⁰. The data in our results showed no difference in cardiomyocyte viability between the α PD1 and α PD1+A77 1726 groups (Supplementary Fig. 5A). These findings indicate that cardioprotective effects of Lef are not dependent on CD8+ T cells or its direct effects on cardiomyocytes.

Lef treatment attenuated intestinal barrier damage in α PD1 mice and its cardioprotective effects are microbiome-dependent

Here, we examined the protective effects of Lef against intestinal injury in α PD1-treated melanoma mice. By comparing the colon length and conducting histological analysis of the small intestine, we found that Lef treatment reversed colon shortening, loss of intestinal villi, and reduction of cuprocytes in the α PD1 group (Supplementary Fig. 6A, B). Furthermore, we detected the expression of tight junction proteins in colonic tissue and found that Lef treatment increased occludin and ZO-1 protein expression in α PD1-treated melanoma mice (Supplementary Fig. 6C). To test our hypothesis that the cardioprotective effects of Lef were dependent on gut microbiota, we performed fecal microbiota transplantation (FMT) (Fig. 4A). Echocardiographic analysis revealed improved cardiac function in mice that received microbiota transplants from α PD1+Lef mice compared to those received transplants from α PD1 mice (Fig. 4B–D). Moreover, mice that received microbiota transplants from α PD1+Lef mice showed reduced levels of BNP, as well as decreased cTnT compared to mice that received transplants from α PD1 mice (Fig. 4E, F). Mice that received α PD1+Lef fecal transplants showed significantly lower myocardial apoptosis than mice that received α PD1 fecal transplants (Fig. 4G). These experiments demonstrate that the cardioprotective effect of Lef was microbiome-dependent.

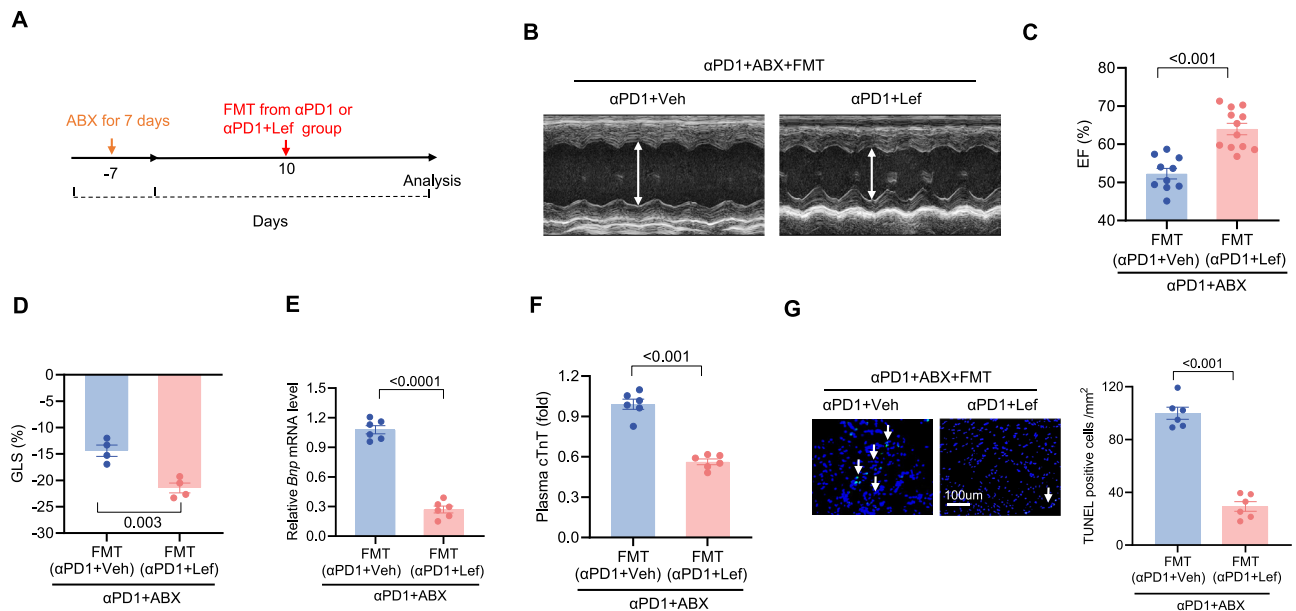


Fig. 4 | Lef ameliorates PD1 inhibitor-induced intestinal barrier dysfunction and the effects of fecal transplantation in mice. **A** Flow chart of fecal microbiota transplantation in α PD1 mice: recipient α PD1 mice, receiving α PD1 mouse feces, and α PD1+Lef mouse feces. Left ventricular end-diastolic dimension (LVIDd) (**B**), Ejection fraction (EF) (**C**), and Global longitudinal strain (GLS) (**D**) were detected in these groups (α PD1: $n = 10$, α PD1+Lef: $n = 12$). **E** Relative mRNA levels of *Bnp* ($n = 6$).

F Plasma biomarker assessments reveal levels of cardiac troponin T (cTnT) ($n = 6$). **G** Terminal deoxynucleotidyl transferase dUTP Nick End Labeling (TUNEL) staining and apoptosis rate in tissues (green, arrows indicate positive signals) ($n = 6$). Nuclei are stained with DAPI (blue). Data are shown as the mean \pm SEM and analyzed using unpaired two-tailed Student's *t*-test.

Lef treatment alters intestinal microbial abundance and community structure in α PD1-treated melanoma mice

Next, to define the impact of Lef on the gut microbiome composition of α PD1-treated melanoma mice, we conducted 16S rRNA analysis on their fecal samples. We employed the Goods coverage index of the dilution curves to assess the adequacy of sequencing. The curves of each group eventually plateaued, indicating sufficient sequencing depth (Fig. 5A). Alpha diversity was utilized to assess microbiota diversity within each group. The results revealed α PD1 and Lef treatment altered microbiota diversity (Fig. 5B). Furthermore, Principal coordinate analysis (PCoA) analysis indicated variations in gut microbiota structure and taxa among the groups (Fig. 5C). Notably, compared to the control group, α PD1 mice exhibited a significant reduction in *Firmicutes* abundance and a notable increase in *Bacteroidota* abundance at the phylum level (Fig. 5D). The alterations of microbial abundance at the genus level were also showed in Supplementary Fig. 7A. The Sankey diagram visually illustrates the shifting distribution of different bacterial groups across the groups, highlighting dynamic changes (Fig. 5E). Furthermore, Lefse analysis identified marked taxonomic distinctions between the α PD1 and α PD1+Lef groups, with notable bacterial species being *Paramuribaculum*, *Oscillospiraceae*, and *Lactobacillus* (Fig. 5F). Subsequent correlation analysis between the genus-level bacterial flora and cardiac function parameters indicated a close relationship between the characteristic bacteria *Paramuribaculum*, *Oscillospiraceae*, and *Firmicutes*, and changes in cardiac function (Fig. 5G).

IPA protected against cardiotoxicity in α PD1-treated melanoma mice

We examined mouse plasma samples using metabolomics and identified a diverse range of metabolites. The major categories were lipid and lipid-like molecules (34.801%), organic acids and derivatives (19.916%), and organoheterocyclic compounds (15.094%) (Fig. 6A). Significant changes in metabolite levels between the groups were observed in the heatmap results. A comparison between the α PD1 group and the control group demonstrated significant differences in 39 metabolites (Fig. 6B).

Conversely, 65 metabolites showed significant changes when comparing the α PD1+Lef group to the α PD1 group (Fig. 6C). The analysis of metabolic pathways indicates the vital role of the tryptophan pathway (Fig. 6D). We then confirmed the necessity of tryptophan in Lef-mediated cardioprotective effects by subjecting mice to a tryptophan deficiency diet (*Trp^{neg}* diet). As expected, Lef treatment did not attenuate cardiotoxicity in α PD1-treated melanoma mice when tryptophan substrates were absent, as suggested by the altered EF and BNP (Fig. 6E, F), indicating the importance of tryptophan-related metabolites in Lef-mediated cardioprotective effects. To reveal the specific metabolite that was responsible for the Lef-mediated cardioprotective effects, a bioinformatics intersection analysis between 16S rRNA analysis and metabolomics was performed. 16S rRNA analysis found that the abundance of 11 genera was statistically altered, and these alterations were prevented by Lef treatment. Metabolomics revealed that 12 representative metabolites were statistically altered, and these alterations were prevented by Lef treatment. We examined the relationship between 12 representative metabolites and 11 genera using correlation analysis. We focused our interest on IPA for the reason that IPA was the only tryptophan-related metabolite. IPA was negatively correlated with *Paramuribaculum*. Moreover, IPA has been shown to promote axonal regeneration²¹ and protect against heart failure with preserved EF²². The volcanic maps also confirmed that IPA was downregulated in the α PD1 group, but upregulated in the α PD1+Lef group (Supplementary Fig. 8A). Following LC-MS/MS analysis of IPA also revealed that plasma and fecal IPA levels were decreased in α PD1-treated melanoma mice, and this reduction was reversed by the treatment of Lef (Supplementary Fig. 8B, C). We observed a significant increase in plasma IPA level in mice that received microbiota transplants from α PD1+Lef mice compared to those receiving transplants from α PD1 mice (Fig. 6H). We also found that there was no significant difference in plasma IPA level between α PD1 and α PD1+Lef groups in *Trp^{neg}* (Supplementary Fig. 8D). We then explored the potential impact of IPA on α PD1-induced cardiotoxicity. The mice were treated with PD1 inhibitors and gavaged with IPA for 2 weeks (Fig. 6I). Subsequent echocardiography revealed IPA improved cardiac function in α PD1-treated melanoma mice (Fig. 6J). The levels of BNP mRNA and

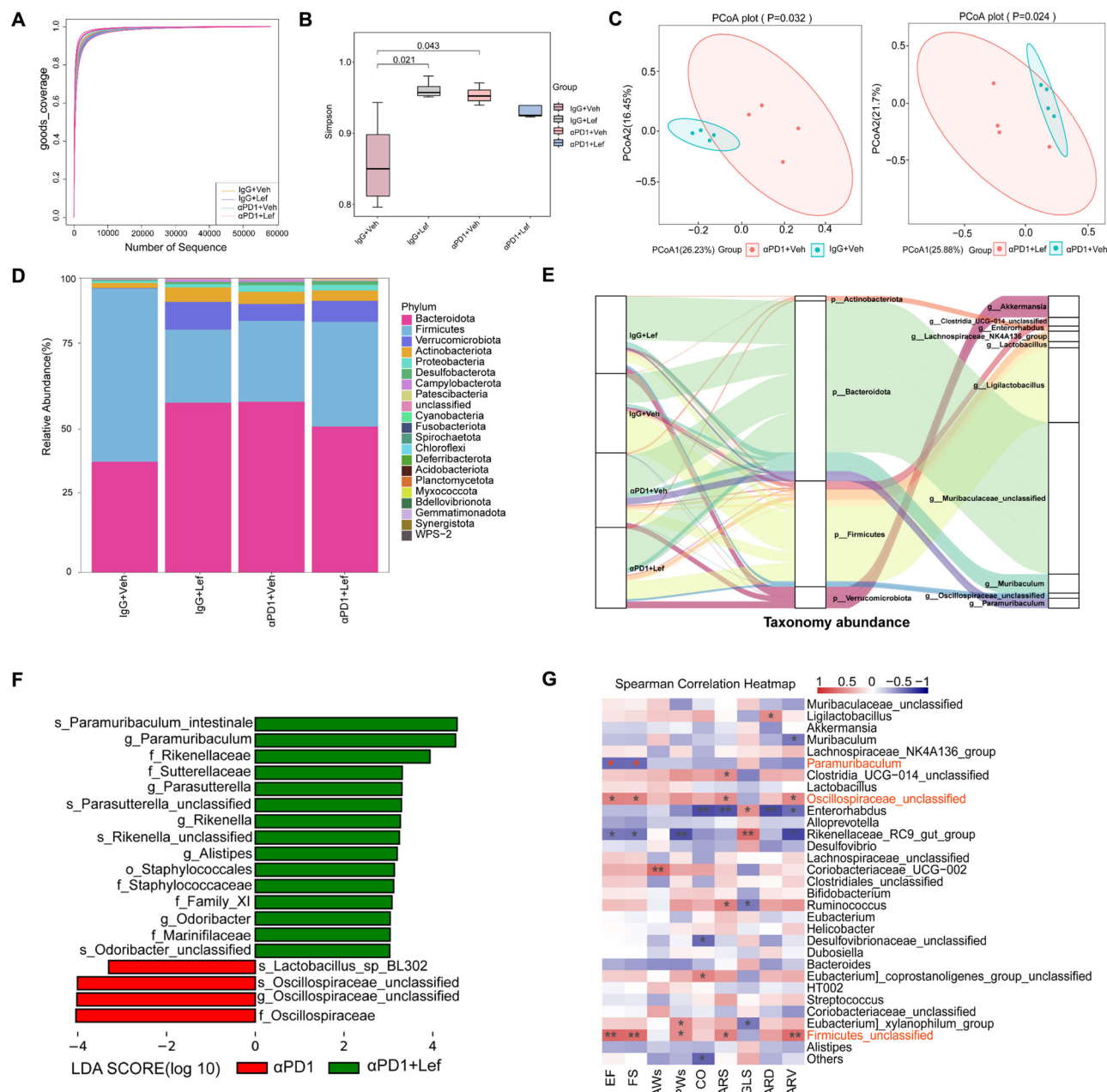


Fig. 5 | Lef treatment alters gut microbial abundance and community structure in PD1 inhibitor-treated mice. A Goods coverage index of dilution curves ($n = 4$). **B** Simpson's index, in response to α -diversity of the flora ($n = 4$). For the box plots, the boxes extend from the first to the third quartile (25th to 75th percentiles), with the center line indicating the median and analyzed using one-way ANOVA followed by Tukey post hoc test (two-sided). **C** Principal coordinate analysis (PCoA), in response to β -diversity of the flora ($n = 4$) (ADONIS test: α PD1 verse IgG, $p = 0.032$;

α PD1 verse α PD1+Lef, $p = 0.024$). **D** Heatmap of clustering of relative abundance of the flora at the phylum level ($n = 4$). **E** Sankey diagram illustrating the dynamic shifts in microbial populations among different groups in response to treatments ($n = 4$). **F** Linear discriminant analysis effect size (LEfSe) analysis of the α PD1 group versus the α PD1+Lef group (LDA threshold = 2.0) ($n = 4$). **G** Pairwise Spearman rank correlation heatmap for the analysis of the relationship between genus-level flora and cardiac function ($n = 4$). Data are shown as the mean \pm SEM.

cardiac enzyme cTnT in mouse hearts showed a notable increase after treatment with a PD1 inhibitor, which was attenuated by the supplementation of IPA (Fig. 6K, L). IPA significantly inhibited α PD1-induced apoptosis in the heart (Supplementary Fig. 8E).

IPA promoted PI3K expression through the ligand binding of AhR in the heart

The pregnane X receptor (PXR) and the AhR are two IPA receptors²³. PXR was not present in the heart²². Recent studies have indicated the significant role of AhR in cardiovascular diseases^{24,25}. Upon activation, AhR enters into the nucleus and binds to its DNA binding site to

promote gene expression²⁶. Western blot revealed AhR expression and its well-defined target cytochrome P450 1A1 (CYP1A1) expression were decreased in response to α PD1, and these downregulations were prevented by the supplementation of IPA (Fig. 7A). These data suggested that IPA-treated mice exhibited increased AhR activation status. To further investigate the role of AhR in IPA-provided cardioprotection against α PD1-induced cardiotoxicity, α PD1 mice were transfected with shAhR (Fig. 7B). Cardiac AhR deficiency almost abolished IPA-provided cardioprotection against α PD1-induced cardiotoxicity, as suggested by the decreased EF and FS, as well as the increased BNP mRNA and cTnT levels. It has been reported that IPA regulates gastrointestinal barrier

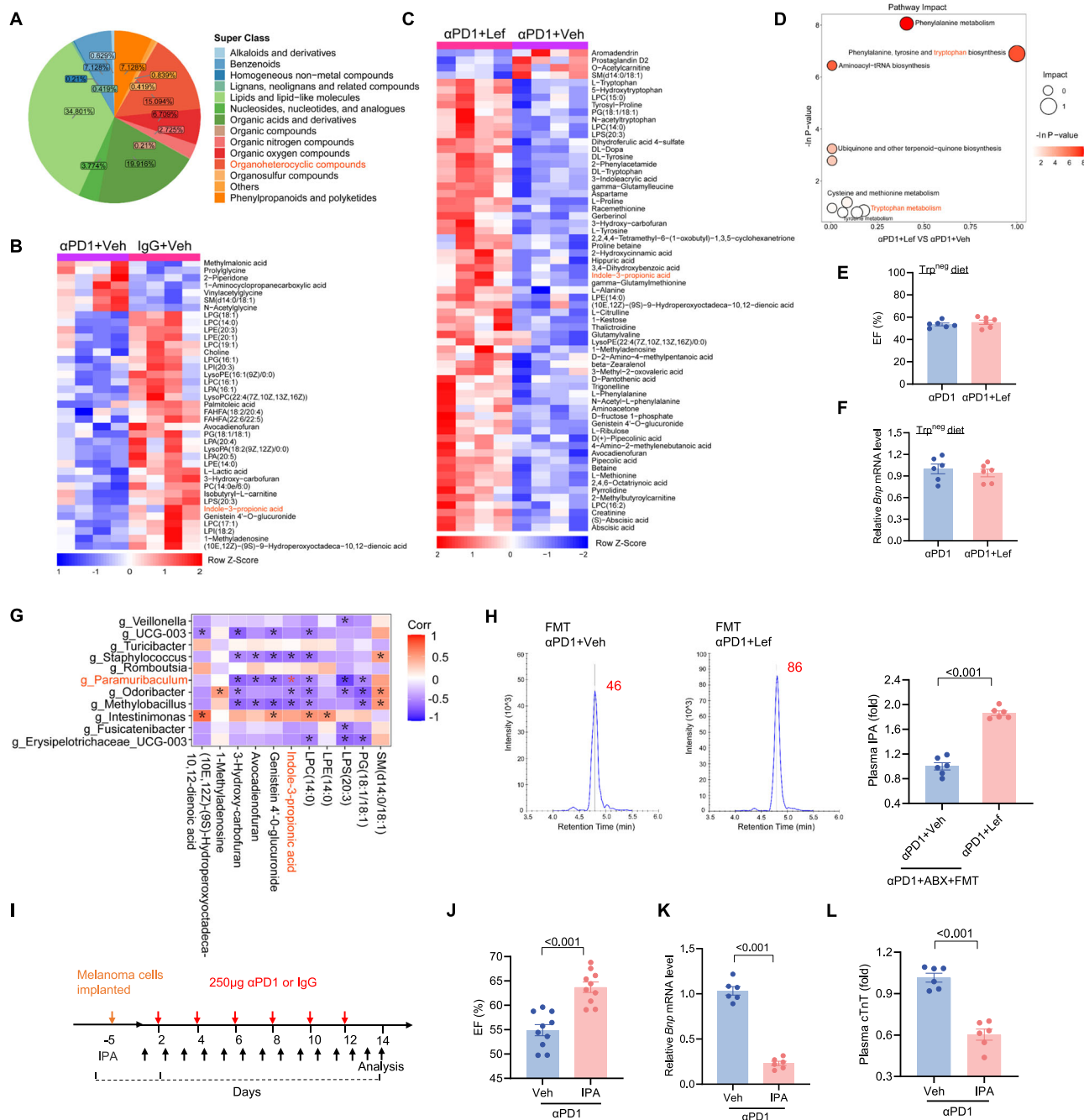


Fig. 6 | IPA protected against cardiotoxicity in α PD1-treated melanoma mice. **A** Metabolite class pie charts. **B**, **C** Clustering heatmap of relative levels of serum metabolites ($n = 4$). **D** Pathway analyses of α PD1+Lef and α PD1+Veh ($n = 4$). Tryptophan deficiency experiments. Ejection fraction (EF) (**E**) and relative mRNA levels of *Bnp* after Tryptophan deficiency (**F**) ($n = 6$). **G** Heatmap of genus-level intestinal

flora in association with characteristic serum metabolites ($n = 4$). **H** Quantitative analysis of IPA ($n = 6$). **I** Mice with 40 mg/kg IPA by gavage for a fortnight. **J** Ejection fraction (EF) ($n = 10$). **K** Relative mRNA levels of *Bnp* ($n = 6$). **L** Plasma biomarker assessments reveal levels of cardiac troponin T (cTnT) ($n = 6$). Data are shown as the mean \pm SEM and analyzed using an unpaired two-tailed Student's *t*-test.

function via PXR and toll-like receptor 4 (TLR4)^{23,27,28}. To further confirm the role of AhR in vitro, adult cardiomyocytes isolated from α PD1-treated melanoma mice were subjected to an AhR inhibitor (CH223191), a PXR inhibitor (resveratrol), or a TLR4 inhibitor (IAXO-102). CH223191, but not resveratrol or IAXO-102, abrogated the protection of IPA on the loss of α PD1 cardiomyocytes (Supplementary Fig. 9A).

To reveal the downstream of IPA and achieve a broader understanding of the impact of IPA on α PD1-induced cardiotoxicity, we analyzed KEGG pathway analysis of RNA-seq data. PI3K-AKT was the most significantly altered signaling pathway. AhR acted as a

transcriptional factor by specifically binding to the C(T)GCGTG motif of target genes²⁹. When searching this motif in the promoter site of PI3K catalytic subunit α , we found that there was one AhR binding site (Fig. 8A). To corroborate this finding, chromatin immunoprecipitation (ChIP)-PCR was performed in the heart, and the results showed enrichment of the PI3K catalytic subunit α promoter region in the AhR precipitate (Fig. 8B). These results suggested that PI3K catalytic subunit α was a direct transcriptional target of AhR. Consistent with these in vitro findings, PI3K catalytic subunit α mRNA level was decreased in α PD1-treated melanoma mice (Fig. 8C, D). Lef or IPA supplementation significantly upregulated the PI3K catalytic subunit α mRNA in IgG or

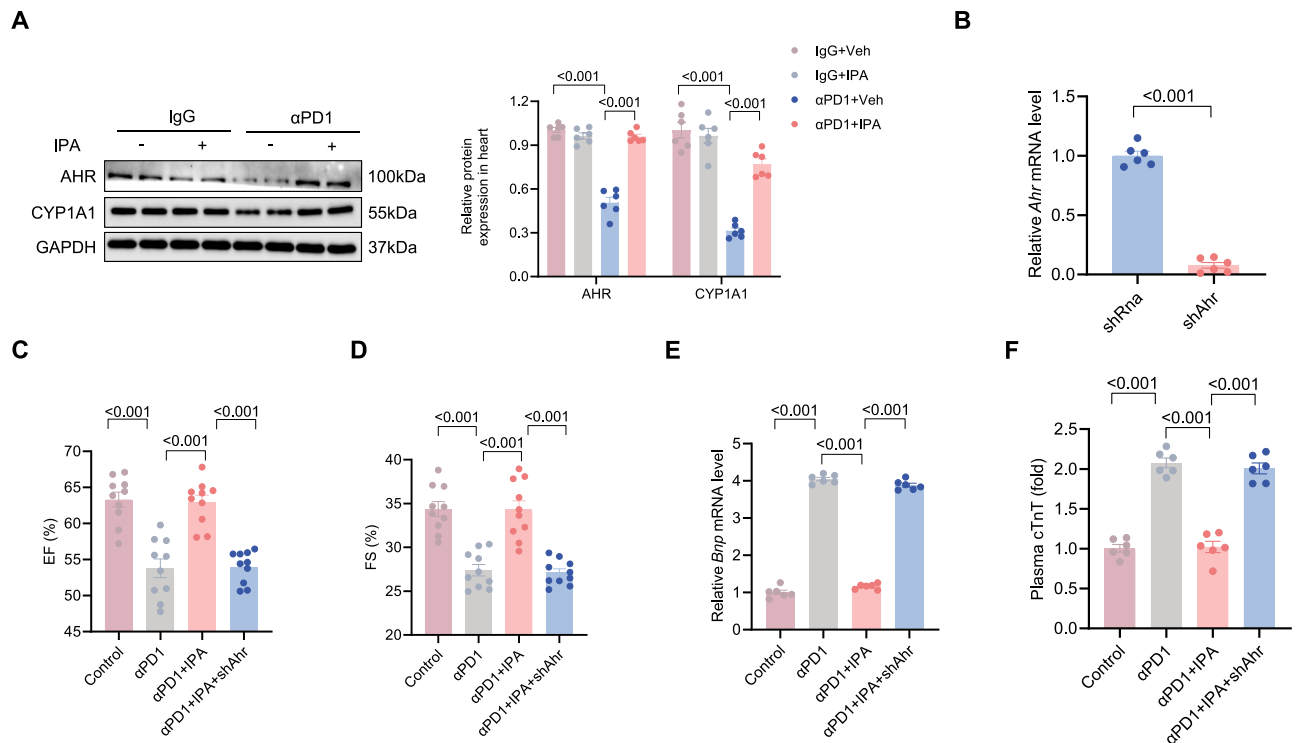


Fig. 7 | IPA affects cardiotoxicity through the AhR receptor. **A** Representative western blots of AhR and CYP1A1 after deficiency of IPA receptor AhR ($n = 6$). **B** Relative mRNA levels of *Ahr* in mouse heart ($n = 6$). Echocardiographic ejection fraction (EF) (**C**) and Fractional shortening (FS) (**D**) ($n = 10$). **E** Relative mRNA levels

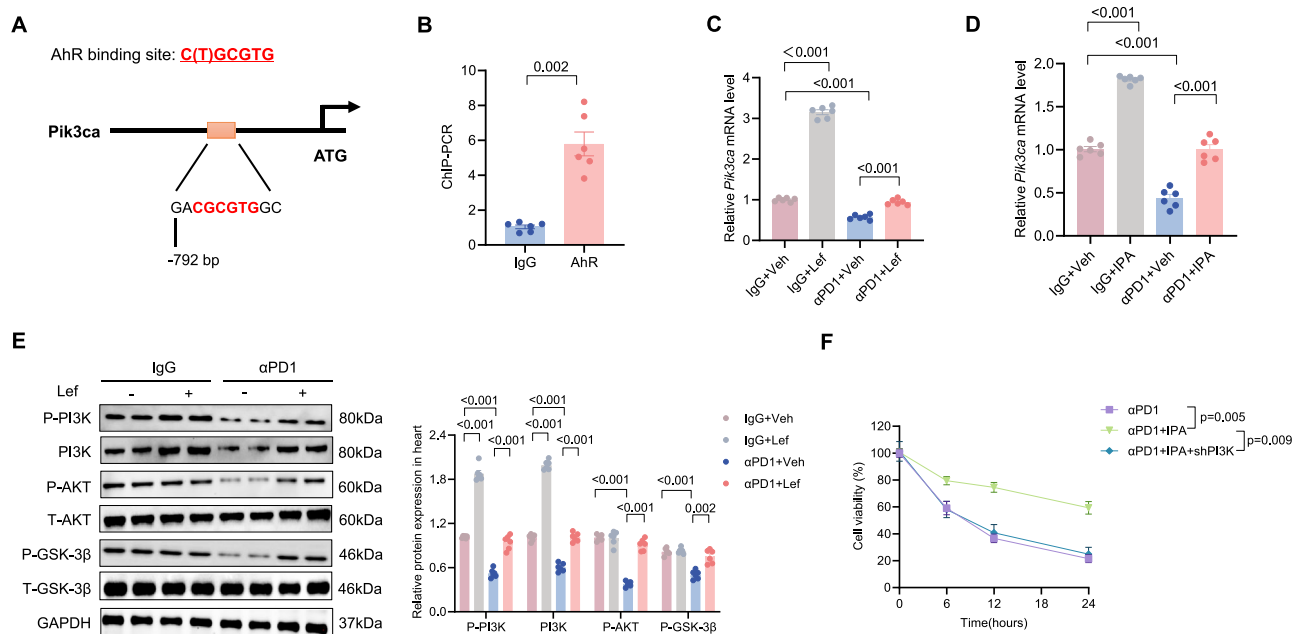


Fig. 8 | IPA promoted PI3K expression through the ligand binding of AhR in the heart. **A** AhR binding site was identified on the PI3K promoter. **B** Independent ChIP-PCR ($n = 6$). **C**, **D** Relative mRNA levels of *Pik3ca* in hearts of mice ($n = 6$). **E** Representative western blots of p-PI3K, PI3K, p-AKT, and p-GSK-3 β protein

α PD1-treated melanoma mice (Fig. 8C, D). We also found that Lef or IPA supplementation significantly upregulated the total and phosphorylated PI3K in IgG or α PD1-treated melanoma mice (Fig. 8E, Supplementary Fig. 10A). The downstream components of the PI3K signaling

pathway, including p-AKT and p-glycogen synthase kinase-3 β (GSK3 β), were decreased in the hearts of α PD1-treated melanoma mice, and these pathological alterations were prevented by the supplementation of Lef or IPA (Fig. 8E, Supplementary Fig. 10A). To establish a causative

relationship between PI3K and cardiomyocytes loss, we performed a PI3K loss-of-function experiment with isolated cardiomyocytes. We found that PI3K deficiency almost abolished the protective effect of IPA on cell viability in vitro (Fig. 8F).

Discussion

Immune checkpoint inhibitors display impressive effectiveness in cancer clinical management. Anti-cytotoxic T-lymphocyte-associated protein 4 (CTLA4) and α PD1 have revolutionized the management of advanced melanoma, for which tumor regression and long-term durable cancer control is nearly 50% of patients, compared with less than 10% historically³⁰. By enhancing T cell function, α PD1 triggers melanoma cell apoptosis. With an increasing use of α PD1 therapy, cardiotoxicity in these patients has been revealed^{31–33}. Thus, it is imperative to explore pharmacological interventions that can effectively suppress α PD1-related cardiotoxicity but not compromise the efficacy of α PD1-mediated immunotherapy. Here, we found that Lef treatment inhibited α PD1-related cardiotoxicity and cardiac apoptosis without compromising the efficacy of α PD1-mediated immunotherapy. This protective effect of Lef was microbiome-dependent, but not T cells dependent. Mechanistically, we identified IPA, which could be applied individually to protect cardiac dysfunction in α PD1-treated melanoma-bearing mice. IPA could directly bind to the AhR and promote the expression of PI3K, thus preventing cardiomyocyte apoptosis in α PD1-treated melanoma-bearing mice.

Emerging evidence from basic and clinical trials has demonstrated that T cell infiltration played a crucial role in the development of α PD1-related cardiotoxicity³⁴. In response to the PD1 inhibitors, T cells are activated and recruited to the cardiac interstitium, where they alter cardiomyocyte function and induce cardiomyocyte apoptosis in a paracrine-dependent manner³⁵. Lef and its active metabolite A77 1726 are known inhibitors of DHODH and are commonly used in clinical settings to treat autoimmune diseases via the inhibition of T cell proliferation, especially rheumatoid arthritis³⁶. Based on these findings, we speculated that Lef treatment might attenuate α PD1-related cardiotoxicity in melanoma-bearing mice. As expected, our results indeed confirmed that Lef administration conferred a protective effect against α PD1-induced cardiotoxicity. The changes in EF and FS are statistically significant but modest. GLS has strong prognostic value for cancer therapy-related cardiac dysfunction³⁷. A significant increase in GLS and ARS were observed in the anterior segments of α PD1+Lef mice compared to those in α PD1 mice. However, in our study, Lef treatment did not have a profound effect on myocardial inflammation, which was in agreement with a previous finding that Lef treatment showed only a moderate or no inhibitory effect on local inflammation infiltration³⁸. Using a monoclonal CD8 antibody, we found that the protection of Lef was independent of its CD8+ T cell-inhibiting capacity. Interestingly, Lef also exhibited a promising anti-tumor property. Lef treatment can hinder the growth of melanoma in mice¹⁶. Furthermore, the combination of Lef with doxorubicin has been shown to effectively inhibit the growth of mammary tumors in mice^{16,39}. These data suggested that Lef treatment might not compromise the inhibitory capacity of α PD1 in tumor mice. As expected, Lef enhanced the efficacy of α PD1-mediated immunotherapy against melanoma progression. All the available data point toward Lef as a promising and effective therapeutic agent against α PD1-related cardiotoxicity in melanoma-bearing mice.

We further explored the mechanisms by which Lef exerts its cardioprotective effects. We found that A77 1726 could not provide direct protection on cardiomyocytes isolated from α PD1-treated mice. Microbiome imbalance has been implicated in the development of various diseases including colitis, coronary heart disease, and hypertension^{12,13,33,40–42}. Cancer patients are particularly vulnerable to microbiota imbalance, due to chemotherapy, radiotherapy, and antibiotic therapy^{43,44}. Melanoma-bearing mice exhibited an improved response to therapy following fecal transplants from

individuals with robust immune responses to PD1 inhibitors, underscoring the significant role of microbiota in PD1 inhibitors treatment⁴⁵. Here, we also found that the intestinal barrier function in α PD1-treated mice was impaired, and these pathological alterations were largely prevented by the supplementation of Lef. Furthermore, 16S rRNA analysis of mouse fecal samples revealed that Lef treatment altered the abundance and community structure of gut microorganisms in α PD1-treated mice, which was in agreement with previous reports that anti-PD-1 immunotherapy altered the diversity and composition of the patient gut microbiome^{46–48}. *Paramuribaculum* was decreased in magnolol-treated pigs, and decreased abundance of *Paramuribaculum* elicited changes in tryptophan metabolism⁴⁹. *Oscillospiraceae* was significantly altered in stool samples of patients receiving allogeneic hematopoietic stem cell transplantation⁵⁰. *Lactobacillus* was decreased in mice with myocardial infarction⁵¹. In our study, we found that *Paramuribaculum*, *Oscillospiraceae*, and *Lactobacillus* were also altered in α PD1-treated mice after Lef treatment. FMT could provide strong evidence to support the contribution of gut microbiota to heart diseases⁵². To confirm the vital role of gut microbiome in Lef-mediated cardioprotective effects, we performed FMT experiments. Mice that received microbiota transplants from α PD1+Lef mice exhibited a better cardiac function compared to those receiving transplants from α PD1 mice, implying that gut microbiome was responsible for the protective effects of Lef treatment against α PD1-related cardiotoxicity.

The gut microbiome functions like an endocrine organ, generating bioactive metabolites and linking with cardiovascular health⁵³. By analyzing metabolomics, we found that the tryptophan pathway was closely involved in α PD1-related cardiotoxicity. Lef lost its protective effects against α PD1-related cardiotoxicity in mice subjected to a tryptophan deficiency diet, indicating the indispensable role of tryptophan-related metabolites in Lef-mediated cardioprotective effects. Consistent with this finding, several genera identified in our study were closely involved in tryptophan synthesis and metabolism. *Paramuribaculum* was decreased in magnolol-treated pigs and played a key role in tryptophan metabolism⁴⁹. Palmitoylethanolamide modulated tryptophan-kynurenine metabolism in the colon through increasing abundance of *Oscillospiraceae*⁵⁴. Bender et al. found that *Lactobacillus* translocated to and persisted within melanoma, affecting dietary tryptophan metabolism⁵⁵. A variety of tryptophan-indole metabolites are derived from bacteria, including IPA, indole-3-acetic acid, and indole-3-acetamide⁵⁶. Here, we found that IPA was decreased in α PD1-treated mice and could be increased by Lef treatment, implying the critical role of IPA in α PD1-related cardiotoxicity. IPA, specifically, could promote nerve regeneration and repair²¹, alleviate atherosclerotic plaque development⁵⁷, and protect against heart failure with preserved ejection fraction²². The impact of IPA on α PD1-related cardiotoxicity has not been reported. In this study, we discovered that IPA improved cardiac function and inhibited cardiac apoptosis in α PD1-treated melanoma-bearing mice. Moreover, IPA enhances immunotherapy efficacy in pan-cancer⁵⁸.

Identification of the cardioprotective role of IPA raised another important question: which factors are responsible for IPA-mediated protection? Here, we found that administration of Lef restored cardiac AhR levels, and IPA acted in the heart by AhR binding and subsequently nuclear translocation to activate the PI3K expression. AhR deficiency largely abolished the protective effects of IPA against α PD1-related cardiotoxicity. The critical role of AhR described in our study was consistent with a previous study that AhR was involved in kynurenine-triggers cardiomyocyte proliferation⁵⁹. Volkova et al. also demonstrated that AhR is cardioprotective against doxorubicin-induced cardiotoxicity⁶⁰. Moreover, we also identified that PI3K was the downstream of AhR after analyzing the RNA-Seq data. We found that AhR could directly bind to the promoter of the PI3K catalytic subunit α

gene and promote its transcription. Interestingly, Lef or IPA treatment significantly increased PI3K protein expression in α PD1-treated melanoma-bearing mice. Given the critical role played by PI3K in cardioprotection⁶¹, PI3K modulation might be a key mechanism by which IPA protects against α PD1-related cardiotoxicity in mice. This hypothesis was verified by our studies assessing the genetic depletion of PI3K, which abolished the protective effects observed in IPA-treated cells.

One of the landmarks of α PD1-related cardiotoxicity is cardiomyocyte death³⁵. Here, we also found that Lef or IPA treatment significantly attenuated α PD1-induced cardiac apoptosis. This anti-apoptotic effect was dependent on the activation of the AhR-PI3K signaling pathway, as supported by the findings that AhR-PI3K deficiency abrogated the protective effects of IPA. The protection provided by Lef was attributed to the attenuation of cardiomyocyte death.

Our study proposes that the microbiota-indole propionic acid-cardiac AHR axis plays a pivotal role in the protective effects of Lef against α PD1-induced cardiotoxicity in mice. The microbiota-IPA-heart axis emerges as a promising target for treating cardiotoxicity in patients receiving immunotherapy.

Methods

Animals and treatment

C57BL/6 mice aged 8–10 weeks were sourced from the Institute of Laboratory Animal Science, Chinese Academy of Medical Sciences (Beijing, China). There were four to six mice per cage, and they were kept in a specific pathogen-free barrier system at a temperature of 20–25 °C, with a 12-h light and 12-h dark cycle, and had ad libitum access to standard laboratory chow. All animal experiments were approved by the Animal Care and Use Committee of Renmin Hospital of Wuhan University (No: WDRM20220509A) and were conducted in accordance with the National Institutes of Health guidelines for the care and use of laboratory animals (NIH publication, revised 2011).

Prior to enrollment, sex-matched C57BL/6 mice were randomly chosen from the sample pool. A suspension was prepared by dissolving 2.5×10^5 B16-F10 cells in 250 μ L PBS, which was then subcutaneously injected into the right side of the mice's abdomen³¹. Tumor volume was measured daily using caliper measurements (length \times width \times height). Starting from 6 days post-tumor transplantation, mice received intraperitoneal injections of 250 μ g/kg of α PD1 (#RMP 1–14, West Lebanon, NH, USA) or an isotype control (#BE0083, West Lebanon, NH, USA) every other day. Starting from 5 days post-tumor transplantation, these mice received a daily dose of 10 mg/kg Lef (#75706, Sigma, St. Louis, MO, USA) for 12 days. The dose of Lef was selected according to our previous study¹⁷. For two IgG-treated groups, $n = 15$ (male = 8; female = 7). For two α PD1-treated groups, $n = 20$ (male = 10; female = 10). To evaluate the impact of Lef on an established melanoma model, starting from 14 days post-tumor transplantation, mice received intraperitoneal injections of α PD1 every other day. At the first time of α PD1 injection, these mice received a daily treatment of Lef. To observe the survival rate of this established melanoma model, we extended the tumor inoculation time to 45 days.

In the CD8⁺ T cells depletion experiment, α PD1-treated melanoma mice were injected intraperitoneally with 400 μ g of CD8 antibody (α CD8, #BE0118, West Lebanon, NH, USA) every other day⁶². The body weight of each mouse was monitored every 2 days. Upon completion of the final Lef treatment, echocardiography examinations were performed. After that, the mice were euthanized, blood samples, tumor specimens, small intestines, colons, and heart tissues were collected for further analysis.

For the IPA treatment experiment, α PD1-treated melanoma mice were orally administered 40 mg/kg IPA (#HYW015229, MedChemExpress, Shanghai, China) for 2 weeks²¹. After the treatment, echocardiography examinations were performed and heart tissues were collected.

For a tryptophan-deficient diet, melanoma-bearing mice in the α PD1 and α PD1+Lef group were given a tryptophan-deficient diet 3 days before α PD1 injection. The diet was maintained for 20 days until the experimental endpoint.

In the cardiac AhR receptor knockdown experiment, mice received a single intravenous injection of adeno-associated virus 9 (AAV9) carrying small hairpin RNA (shRNA) against AhR under the cTnT promoter via the tail vein at a concentration of 1×10^{11} viral genome per mouse⁹. The shRNA sequence used is AATAA-CACTTCTACAGACCTAAA. The specific shAhR sequence used is as follows: 5'-CCGGCATCGACATAACGGACGAAATCTCGAGATTTCGTC CGTTATGTGCGATGTTTTTG-3'. Three weeks post-AAV9 injection, these melanoma-bearing mice were exposed to repeated α PD1 injections.

Fecal microbial transplantation

Mice were administered broad-spectrum antibiotics (including vancomycin 0.5 g/L, neomycin sulfate 0.5 g/L, and purine 0.5 g/L) in their drinking water for 1 week to deplete their intestinal flora⁶³. Subsequently, fresh fecal samples were obtained from α PD1+Lef mice or α PD1 mice at 08:00 local time by transferring them to clean cages and collecting 1 g of feces using sterile forceps. The fecal samples were homogenized in 10 mL PBS by vortexing, then centrifugation at 3000 rpm for 30 s at 4 °C. The supernatant was transferred to a new tube and centrifuged at 12,000 rpm for 5 min at 4 °C. Finally, the bacterial precipitate was resuspended in 2.5 mL of PBS. FMT was performed via an oral gavage at a dose of 200 μ L per mouse around 11:00 local time⁶⁴.

Isolation of adult mouse cardiomyocytes

After euthanizing the mice, heart samples were obtained through sterile surgery. Subsequently, the collected hearts were pre-cooled at 4 °C in Ca²⁺-free Tyrode's solution before being transferred to the Langendorff isolated heart perfusion apparatus. The hearts were then submerged in calcium-free perfusion buffer and perfused for 3 min, followed by digestion with 1.5 g/L type II collagenase for 10 min. Following digestion, the hearts were minced into pieces of ~1 mm³ in size. Cell isolation from the mouse hearts was carried out to accurately separate cardiomyocytes, endothelial cells, and cardiac fibroblasts as previously described⁶⁵. To verify the purity, the morphology of adult cardiomyocytes was observed using an inverted microscope, and cardiomyocytes were stained for α -actinin using immunofluorescence.

Cell cultures and treatments

The B16-F10 cells of mouse melanoma were obtained from the Cell Bank of the Chinese Academy of Sciences (Shanghai, China) and were cultured in RPMI Medium 1640 (#11875119, Gibco) supplemented with 10% FBS. Cell proliferation was assessed using the CCK-8 assay kit (C0038, Beyotime, China)⁶⁶.

Cardiomyocytes from the α PD1 group were isolated by perfusion and inoculated into 96-well plates at a density of 3000 cells per well. Next, the cells were treated with A771726 (100 μ M, dissolved in 0.1% DMSO) (SML0936, Sigma-Aldrich, St. Louis, MO, USA) or an equal volume of DMSO¹⁷. After incubation for 24 h, 10 μ L CCK-8 reagent was added to each well. Subsequently, the optical density values were measured at 450 nm using a SYNERGY H4 enzyme labeler.

Cardiomyocytes isolated from the α PD1 group at a concentration of 3000 cells per well were plated in 96-well plates with 100 μ L of DMEM/F12 medium containing 10% FBS along with IPA (20 μ M, dissolved in 0.1% DMSO). To knock down the expression of PI3K, cells were transfected with adenoviral genome particles carrying shRNA against PI3K (MOI = 50)^{67,68}. After incubation for 24 h, 10 μ L CCK-8 reagent was added to each well. OD values were then determined at 450 nm using a SYNERGY H4 enzyme labeler.

Cardiomyocytes isolated from the α PD group were seeded into a 96-well plate at a concentration of 3000 cells per well. The cells were divided into the following groups: α PD1, α PD1+IPA (20 μ M), α PD1+IPA+CH223191 (5 μ M, #HY-12684, MedChemExpress), α PD1+IPA+Resveratrol (10 μ M, #HY-16561, MedChemExpress), and α PD1+IPA+IAXO-102 (5 μ M, #HY-125171, MedChemExpress).

Echocardiography and high-frequency speckle-tracking analysis

Mice were anesthetized with 1.5% isoflurane and echocardiography was then conducted using the Vevo[®] 3100 High-Resolution Preclinical Imaging System (FUJIFILM Visual Sonics) to comprehensively assess both overall and localized cardiac dynamics after α PD1 injection¹⁷. Cardiac function parameters, such as left ventricular EF and FS, were measured using short-axis M-mode analysis to acquire cardiac cycles. Additionally, GLS, ARS, along with their corresponding displacements and velocities, were assessed using M-mode. These parameters were evaluated across three to four cardiac cycles, encompassing EF, FS, left ventricular end-systolic internal diameter (LVIDs), LVIDd, left ventricular anterior systolic wall thickness (LVAWs), left ventricular posterior wall thickness (LVPWs), HR, and CO. Left ventricular strain was assessed using a speckle-tracking algorithm, with strain indicating myocardial tissue deformation.

Western blot analysis

Proteins were extracted from α PD1 and control mouse heart tissues using a lysis buffer containing a mixture of protease inhibitor cocktail (#11852700, Roche, Basel, Switzerland) and phosphatase inhibitor (#04906837001, Roche, Basel, Switzerland). Protein concentrations were determined using the BCA assay kit (#23227, Invitrogen). The proteins were electrophoresed on SDS-PAGE (10% or 12% gel) and transferred to polyvinylidene fluoride membranes (#IPFL00010, Millipore, MA, USA) following established methods⁶⁹. After a 2-h sealing period with a 5% skimmed milk solution, the membranes underwent overnight incubation at 4 °C with primary antibodies: anti-Bax (#2772, Cell Signaling Technology, Danvers, MA, USA), anti-Bcl-2 (#3498, Cell Signaling Technology, Danvers, MA, USA), anti-occludin (#27260-1-AP, Proteintech, Manchester, UK), anti-ZO-1 (#TA5145, Abmart, Shanghai, China), anti-AhR (#83200, Cell Signaling Technology, Danvers, MA, USA), anti-cytochrome P450 1A1 (#94004, Cell Signaling Technology, Danvers, MA, USA), anti-phospho-PI3K(#27921-1-AP, Proteintech, Manchester, UK), anti-PI3K(#20662-1-AP, Proteintech, Manchester, UK), anti-phospho-AKT (#4060, Cell Signaling Technology, Danvers, MA, USA), anti-AKT (#9272, Cell Signaling Technology, Danvers, MA, USA), anti-phospho-GSK (#9323, Cell Signaling Technology, Danvers, MA, USA), anti-GSK-3 β (#12456, Cell Signaling Technology, Danvers, MA, USA) and anti-GAPDH (#2118, Cell Signaling Technology, Danvers, MA, USA). Subsequently, the membranes were incubated with secondary antibodies conjugated with horseradish peroxidase for a period of 1.5 h at room temperature. Blot visualization was performed using an enhanced chemiluminescence kit (#1705061, Bio-Rad Laboratories, Hercules, USA) and the resulting images were analyzed utilizing ImageJ software (NIH, Bethesda, MD, USA).

Quantitative real time-PCR

RNA extraction was performed on cardiac tissue samples obtained from α PD1 and control mouse heart tissues. The Trizol reagent (#15596-026, Invitrogen) was utilized to extract RNA from the cardiac tissue according to the provided instructions. cDNA fragments were generated using the Transcription First Strand cDNA Synthesis Kit (#04896866001, Roche Diagnostics, Basel, Switzerland) and amplified on the Roche Light Cycler[®] 480 detection system. The SYBR Green PCR Kit (#04707516001, Roche) was used for amplification on the detection system. The primer sequences can be found in the Supplementary Table 1, and GAPDH was used as the endogenous reference gene in this study.

Histological analysis

Heart and small intestine tissues were fixed in a 10% neutral formalin buffer overnight. Following dehydration and paraffin embedding, the tissues were cut into 4.0 μ m thick sections with a slide slicer (Leica, Nussloch, Germany). After deparaffinization with xylene, the sections were subjected to hematoxylin and eosin (H&E) staining to evaluate the cross-sectional area in the cardiac tissue and damage to the small intestinal mucosa. The general morphology of the heart and small intestine was observed under a light microscope, and the data were analyzed using a digital analysis software (Image-Pro Plus 6.0, Media Cybernetics, Bethesda, USA).

For Masson's trichrome staining, paraffin sections were initially treated with xylene to eliminate paraffin, and then dehydrated in graded ethanol. Subsequently, the sections were stained with Masson's trichrome using a commercial kit (#G1006, Servicebio, China). Assessment of cardiac fibrosis and collagen deposition was performed under a microscope. ImageJ software was employed to quantify the extent of fibrosis and collagen deposition. All the slides were examined by two authors in a blinded manner.

Immunofluorescence and TUNEL staining

Following formalin fixation and paraffin embedding, neoplastic specimens were meticulously sectioned into 5 μ m slices. Cardiac and neoplastic tissues were processed for immunofluorescence characterization in accordance with methodologies delineated in our previous study⁷⁰. In summary, the slides underwent deparaffinization in xylene and sequential rehydration. Antigen retrieval preceded the application of a blocking solution comprising 10% goat serum in PBS and incubated for 1.5 h at 37 °C. Following the blocking step, the cardiac and neoplastic specimens were incubated with monoclonal anti-CD4 (#ab133616, Abcam, Cambridge, USA), anti-CD8 (#ab217344, Abcam), and anti-Ki67 (#ab15580, Abcam) at 4 °C overnight. Subsequent to primary antibodies incubation, heart and tumor sections underwent PBS washing to remove unbound antibodies, followed by incubation with Alexa Fluor 488 conjugated anti-rabbit IgG secondary antibody (#A21206, Invitrogen, USA) for 2 h within a controlled environment heated to 37 °C. The final step entailed nuclear counterstaining employing DAPI (#S36939, Invitrogen, USA) for a brief interlude of 3 min. Fluorescent images were then acquired using a dedicated fluorescence imaging system.

Terminal deoxynucleotidyl transferase dUTP nick end labeling (TUNEL) assay was employed for the visualization of apoptotic nuclei in cardiac sections, utilizing a commercially available kit (Billerica, USA). Quantification of apoptosis involved the computation of the proportion of TUNEL-positive nuclei to the total number of DAPI-stained nuclei.

Biochemical analysis

Levels of cardiac injury markers, including cTnT and CK-MB were quantified in heart tissue samples using commercially available kits (Nanjing Jiancheng Bioengineering Institute, Nanjing, China), following the recommended protocols provided by the manufacturer.

Flow cytometry

The tumor tissues were isolated from the mice, and any surface hair was carefully removed. The tumor tissues were washed repeatedly with PBS buffer to eliminate blood crusts. After that, these tumor tissues were incubated with the RPMI-1640, containing 1 mg/mL collagenase D, 0.1 mg/mL hyaluronidase, and 0.2 mg/mL DNase I at 37 °C for 60 min. Then we filtered the digested tissue mixture through a cell strainer. After centrifugation at 300 \times g for 5 min at 4 °C, the cell suspension was reacted with a lymphocyte separation medium. The layer located at the interface was collected and washed repeatedly. This suspension was incubated with 2 μ L of the FcX blocking reagent (BD Pharmingen, USA). APC-Cy7 Rat Anti-Mouse CD45 (30-F11, #57659, BD

Pharmingen, USA), PE-Cy7 Rat Anti-Mouse CD8a (53-6.7, #552877, BD Pharmingen), MsCD3e APC 145-2C11 (#553066, BD Pharmingen), and PE Rat Anti-Mouse CD4 (RM 4-5, #553048, BD Pharmingen) were utilized for staining. Additionally, 7-AAD (559925, BD Pharmingen) was employed for distinguishing between dead and live cells. CytoFLEX flow cytometer (Beckman Coulter) was used for flow cytometry and data were analyzed using FlowJo software v10.0.

Preparation of fecal samples and 16S rRNA sequencing

At the endpoint of the experiment, one mouse was put in a cage and then four biological replicate fecal samples were collected using a sterile process. fecal samples Fresh feces were promptly collected into labeled sterile EP tubes, aiming for a minimum of 80 mg per mouse. If necessary, defecation was induced by gentle abdominal massage. The collected samples were quickly frozen in liquid nitrogen and stored at -80°C for downstream analysis. Microbial analysis was conducted using 16S rRNA gene sequencing on the Illumina platform with a double-ended sequencing approach. DNA extraction from four stool samples per group was performed according to the protocol of TIA-Namp Bacterial Kit (Tiangen Biochemical Technology, Beijing, China). Subsequently, PCR amplification of the V3-V4 region of the bacterial 16S rRNA gene was carried out using the 338F (5'-ACTCCTACGG-GAGGAGCA-3') and 806R (5'-GGACTACHVGGGTWTCTAAT-3') primers. The resulting amplicons were purified using AmpureXP microbeads and eluted in an elution buffer. Finally, the purified V3-V4 amplicons underwent sequencing on the Illumina platform. Raw 16S rRNA gene amplicons were processed and assembled using the Overlap software (v1.31.2) to ensure high sequencing quality. These high-quality amplicons were then classified based on the Amplicon Sequence Variant (ASV) using the QIIME package and reference databases including QIIME v1.9.1 and the Greengenes database v201305. Taxonomic profiles were generated at multiple levels (phylum, class, order, family, genus) based on ASV annotation. To assess the richness of gut microbial communities, various α -diversity indices such as Simpson's Diversity Index were employed. Differences in the overall composition and structure of the microbiota among the four groups were analyzed using principal coordinates analysis (β diversity) based on ASV abundance. 16S rRNA sequencing and subsequent analyses were performed by Biotree (Shanghai, China).

Metabolomics

We employed liquid chromatography-tandem mass spectrometry (LC-MS/MS) (Biotree Biotech Co., Ltd, Shanghai) for metabolomics studies. We used four biological replicate plasma samples. Then plasma samples were thawed in ice water, vortexed, and mixed with 200 μL water plus 1200 μL 1:1 acetonitrile-methanol (containing isotopes). After 30 s vortexing and 15 min ice-bath sonication, they were incubated at -40°C for 2hs, then centrifuged at 12,000 rpm, 4°C for 15 min. The 1200 μL supernatant was transferred, evaporated in a concentrator, and reconstituted with 120 μL 60% acetonitrile post-vortexing and centrifugation. Ultimately, 60–70 μL aliquots were placed in glass vials for LC-MS/MS analysis. Plasma metabolites were analyzed using untargeted LC-MS/MS. The LC-MS/MS analyses were carried out using a UHPLC system (Vanquish, Thermo Fisher Scientific) equipped with a Phenomenex Kinetex C18 column (2.1 \times 50 mm, 2.6 μm), coupled to an Orbitrap Exploris 120 mass spectrometer (Orbitrap MS, Thermo). Following the detection of serum metabolites, orthogonal projections using Orthogonal Partial Least Squares Discriminant Analysis (OPLS-DA) were employed to explore the overall distribution of plasticity metabolites and identify differential metabolites between the αPD1 and $\alpha\text{PD1+Lef}$ groups. Differential serum metabolites were identified based on a combined criterion of fold change (>1.2) and p value (<0.05). Data processing was performed using a customized procedure developed in R and based on XCMS. Finally, the metabolites were annotated utilizing an in-house MS2

database (BiotreeDB). IPA was detected on an AB Sciex QTrap 6500 plus mass spectrometer (SCIEX, Framingham, MA, USA). Standard ion source settings included: IonSpray Voltage at +5000 V, Curtain Gas at 35 psi, Temperature maintained at 400°C , and both Ion Source Gas 1 and Gas 2 set to 60 psi. Data processing for LC-MS/MS was carried out using Skyline Software.

Transcriptome sequencing of heart tissue

After undergoing cardiac ultrasound, αPD1 , $\alpha\text{PD1+Lef}$, and control mice were euthanized, and total RNA was extracted using a Trizol reagent. The purity and concentration of the RNA were assessed using a NanoDrop spectrophotometer (Thermo Scientific), while its integrity and quantity were measured using an Agilent 2100/4200 RNA spectrophotometer (Thermo Scientific). Library construction was carried out using the NEBNext[®] Ultra[™] RNA Library Prep Kit for Illumina[®] (NEB, USA), with 3 μg RNA per sample, following the manufacturer's recommendations. Subsequently, the library preparations were sequenced on the Illumina HiSeq platform to generate paired-end reads, following clustering with the TruSeq PE Cluster Kit v3-cBot-HS (Illumina). Four independent biological replicates were sequenced separately for each group. After removing low-quality reads using fastp (v0.21.0), the filtered reads were mapped to the reference genome using HISAT2. Significantly differentially expressed transcripts were screened by applying the criterion fold change ≥ 2 or ≤ -2 and p value ≤ 0.05 . The DEGs between the two groups was analyzed using the DESeq2 R package. To assess the statistically significant enrichment of DEGs in KEGG pathways, we employed the ClusterProfiler software (v3.18.1), applying a padj (False Discovery Rate, FDR) < 0.05 . RNA-seq and subsequent analyses were performed by Bioyi Biotechnology Co., Ltd (Wuhan, China).

ChIP-PCR assay

ChIP assays were carried out using the Upstate EZ ChIP kit (Upstate Biotechnology) following the manufacturer's instructions. Briefly, heart tissues were homogenized and fragmented overnight. Immunoprecipitation was then carried out at 4°C using an anti-AhR antibody. To enhance binding, 20 μL ChIP Grade Protein A/G Plus Agarose was added and incubated for an additional hour at 4°C with gentle agitation. Following this, protein-DNA complexes were recovered, crosslinks were reversed, and the purified DNA was subjected to PCR analysis for further investigation.

Statistics

The data are presented as the mean value \pm the standard error of the mean (SEM). The number of samples (n) represents biological replicates. No samples were excluded from the analysis. Data were considered statistically significant if the p value was less than 0.05. Comparisons among more than two groups were performed by one-way ANOVA followed by the post hoc Tukey test for multiple comparisons when the data had a normal distribution and ANOVA found no variance inhomogeneity; otherwise, Tamhane's T2 post hoc test was used (GraphPad Prism, version 9.0). Differences between the two groups were analyzed by two-tail unpaired t -test. The dominance of bacterial communities among taxa was assessed using linear discriminant analysis (LDA), and effect sizes were analyzed using an LDA score (log 10) of 2.0 as the critical value.

Reporting summary

Further information on research design is available in the Nature Portfolio Reporting Summary linked to this article.

Data availability

The data that support the main findings are available within the main text and the supplementary, and Source data. The datasets generated for the RNA-seq are available through the Gene Expression Omnibus

(<https://www.ncbi.nlm.nih.gov/geo/query/acc.cgi?acc=GSE286252>). The 16S rRNA sequence datasets in this study were deposited at the NCBI under the accession code PRJNA1204802 (<https://www.ncbi.nlm.nih.gov/bioproject/1204802>). The metabolomics data were deposited in the MetaboLights (<https://www.ebi.ac.uk/metabolights/MTBLS12066>). Source data are provided with this paper.

References

- Turner, N., Ware, O. & Bosenberg, M. Genetics of metastasis: melanoma and other cancers. *Clin. Exp. Metastasis* **35**, 379–391 (2018).
- Siegel, R. L., Miller, K. D., Fuchs, H. E. & Jemal, A. Cancer statistics, 2022. *CA A Cancer J. Clin.* **72**, 7–33 (2022).
- Robert, C. et al. Five-year outcomes with dabrafenib plus trametinib in metastatic melanoma. *N. Engl. J. Med.* **381**, 626–636 (2019).
- Hodi, F. S. et al. Improved survival with ipilimumab in patients with metastatic melanoma. *N. Engl. J. Med.* **363**, 711–723 (2010).
- Woo, T. E. et al. Effectiveness of immune checkpoint inhibitor with anti-PD-1 monotherapy or in combination with ipilimumab in younger versus older adults with advanced melanoma. *Curr. Oncol.* **30**, 8936–8947 (2023).
- Krishnamoorthy, M., Lenehan, J. G. & Maleki Vareki, S. Neoadjuvant immunotherapy for high-risk, resectable malignancies: scientific rationale and clinical challenges. *J. Natl. Cancer Inst.* **113**, 823–832 (2021).
- Wu, Y., Xu, Y. & Xu, L. Drug therapy for myocarditis induced by immune checkpoint inhibitors. *Front. Pharmacol.* **14**, 1161243 (2023).
- Arangalage, D. et al. Survival after fulminant myocarditis induced by immune-checkpoint inhibitors. *Ann. Intern. Med.* **167**, 683–684 (2017).
- Okazaki, T. et al. Autoantibodies against cardiac troponin I are responsible for dilated cardiomyopathy in PD-1-deficient mice. *Nat. Med.* **9**, 1477–1483 (2003).
- Quagliariello, V. et al. NLRP3 as putative marker of ipilimumab-induced cardiotoxicity in the presence of hyperglycemia in estrogen-responsive and triple-negative breast cancer cells. *Int. J. Mol. Sci.* **21**, 7802 (2020).
- Quagliariello, V. et al. Combinatorial immune checkpoint blockade increases myocardial expression of NLRP-3 and secretion of H-FABP, NT-pro-BNP, interleukin-1 β and interleukin-6: Biochemical implications in cardio-immuno-oncology. *Front. Cardiovasc. Med.* **11**, 1232269 (2024).
- Witkowski, M., Weeks, T. L. & Hazen, S. L. Gut microbiota and cardiovascular disease. *Circ. Res.* **127**, 553–570 (2020).
- Battson, M. L. et al. Gut microbiota regulates cardiac ischemic tolerance and aortic stiffness in obesity. *Am. J. Physiol. Heart Circ. Physiol.* **317**, H1210–H1220 (2019).
- Zhang, Y. et al. Hormonal therapies up-regulate MANF and overcome female susceptibility to immune checkpoint inhibitor myocarditis. *Sci. Transl. Med.* **14**, eabo1981 (2022).
- Liang, C. et al. HIF1 α inhibition facilitates Leflunomide-AHR-CRP signaling to attenuate bone erosion in CRP-aberrant rheumatoid arthritis. *Nat. Commun.* **10**, 4579 (2019).
- White, R. M. et al. DHODH modulates transcriptional elongation in the neural crest and melanoma. *Nature* **471**, 518–522 (2011).
- Ma, Z.-G. et al. A77 1726 (leflunomide) blocks and reverses cardiac hypertrophy and fibrosis in mice. *Clin. Sci.* **132**, 685–699 (2018).
- Awadalla, M. et al. Global longitudinal strain and cardiac events in patients with immune checkpoint inhibitor-related myocarditis. *J. Am. Coll. Cardiol.* **75**, 467–478 (2020).
- Bonaca, M. P. et al. Myocarditis in the setting of cancer therapeutics: proposed case definitions for emerging clinical syndromes in cardio-oncology. *Circulation* **140**, 80–91 (2019).
- Vrenken, T. E., Buist-Homan, M., Kalsbeek, A. J., Faber, K. N. & Moshage, H. The active metabolite of leflunomide, A77 1726, protects rat hepatocytes against bile acid-induced apoptosis. *J. Hepatol.* **49**, 799–809 (2008).
- Serger, E. et al. The gut metabolite indole-3 propionate promotes nerve regeneration and repair. *Nature* **607**, 585–592 (2022).
- Wang, Y.-C. et al. Indole-3-propionic acid protects against heart failure with preserved ejection fraction. *Circ. Res.* **134**, 371–389 (2024).
- Roager, H. M. & Licht, T. R. Microbial tryptophan catabolites in health and disease. *Nat. Commun.* **9**, 3294 (2018).
- Vilahir, G. et al. Reperfusion-triggered stress protein response in the myocardium is blocked by post-conditioning. Systems biology pathway analysis highlights the key role of the canonical aryl-hydrocarbon receptor pathway. *Eur. Heart J.* **34**, 2082–2093 (2013).
- Chen, H. et al. Perfluorooctane sulfonamide (PFOSA) induces cardiotoxicity via aryl hydrocarbon receptor activation in zebrafish. *Environ. Sci. Technol.* **56**, 8438–8448 (2022).
- Zelante, T. et al. Tryptophan catabolites from microbiota engage aryl hydrocarbon receptor and balance mucosal reactivity via interleukin-22. *Immunity* **39**, 372–385 (2013).
- Flannigan, K. L. et al. The pregnane X receptor and indole-3-propionic acid shape the intestinal mesenchyme to restrain inflammation and fibrosis. *Cell. Mol. Gastroenterol. Hepatol.* **15**, 765–795 (2023).
- Xiao, H. et al. Gut microbiota-derived indole 3-propionic acid protects against radiation toxicity via retaining acyl-CoA-binding protein. *Microbiome* **8**, 69 (2020).
- Denison, M. S. & Nagy, S. R. Activation of the aryl hydrocarbon receptor by structurally diverse exogenous and endogenous chemicals. *Annu. Rev. Pharmacol. Toxicol.* **43**, 309–334 (2003).
- Carlino, M. S., Larkin, J. & Long, G. V. Immune checkpoint inhibitors in melanoma. *Lancet* **398**, 1002–1014 (2021).
- Michel, L. et al. Targeting early stages of cardiotoxicity from anti-PD1 immune checkpoint inhibitor therapy. *Eur. Heart J.* **43**, 316–329 (2022).
- Raschi, E. et al. Cardiovascular toxicity of immune checkpoint inhibitors: a guide for clinicians. *Drug Saf.* **46**, 819–833 (2023).
- Lyon, A. R., Yousaf, N., Battisti, N. M. L., Moslehi, J. & Larkin, J. Immune checkpoint inhibitors and cardiovascular toxicity. *Lancet Oncol.* **19**, e447–e458 (2018).
- Restifo, N. P., Dudley, M. E. & Rosenberg, S. A. Adoptive immunotherapy for cancer: harnessing the T cell response. *Nat. Rev. Immunol.* **12**, 269–281 (2012).
- Moslehi, J. J., Salem, J.-E., Sosman, J. A., Lebrun-Vignes, B. & Johnson, D. B. Increased reporting of fatal immune checkpoint inhibitor-associated myocarditis. *Lancet* **391**, 933 (2018).
- Fragoso, Y. D. & Brooks, J. B. B. Leflunomide and teriflunomide: altering the metabolism of pyrimidines for the treatment of autoimmune diseases. *Expert Rev. Clin. Pharmacol.* **8**, 315–320 (2015).
- Oikonomou, E. K. et al. Assessment of prognostic value of left ventricular global longitudinal strain for early prediction of chemotherapy-induced cardiotoxicity: a systematic review and meta-analysis. *JAMA Cardiol.* **4**, 1007–1018 (2019).
- Luo, Q. et al. A novel disease-modifying antirheumatic drug, iguratimod, ameliorates murine arthritis by blocking IL-17 signaling, distinct from methotrexate and leflunomide. *J. Immunol.* **191**, 4969–4978 (2013).
- Brown, K. K., Spinelli, J. B., Asara, J. M. & Toker, A. Adaptive reprogramming of de novo pyrimidine synthesis is a metabolic vulnerability in triple-negative breast cancer. *Cancer Discov.* **7**, 391–399 (2017).
- Gong, B. et al. Immune checkpoint inhibitors in cancer: the increased risk of atherosclerotic cardiovascular disease events and progression of coronary artery calcium. *BMC Med.* **22**, 44 (2024).
- Cui, B. et al. Effects of chronic noise exposure on the microbiome-gut-brain axis in senescence-accelerated prone mice: implications for Alzheimer's disease. *J. Neuroinflamm.* **15**, 190 (2018).

42. Yadav, J. et al. Gut microbiome modified by bariatric surgery improves insulin sensitivity and correlates with increased brown fat activity and energy expenditure. *Cell Rep. Med.* **4**, 101051 (2023).
43. Di Modica, M. et al. Gut microbiota condition the therapeutic efficacy of trastuzumab in HER2-positive breast cancer. *Cancer Res.* **81**, 2195–2206 (2021).
44. Joachim, L. et al. The microbial metabolite desaminotyrosine enhances T-cell priming and cancer immunotherapy with immune checkpoint inhibitors. *EBioMedicine* **97**, 104834 (2023).
45. Routy, B. et al. Gut microbiome influences efficacy of PD-1-based immunotherapy against epithelial tumors. *Science* **359**, 91–97 (2018).
46. Matson, V., Chervin, C. S. & Gajewski, T. F. Cancer and the microbiome-influence of the commensal microbiota on cancer, immune responses, and immunotherapy. *Gastroenterology* **160**, 600–613 (2021).
47. Pushalkar, S. et al. The pancreatic cancer microbiome promotes oncogenesis by induction of innate and adaptive immune suppression. *Cancer Discov.* **8**, 403–416 (2018).
48. Gopalakrishnan, V. et al. Gut microbiome modulates response to anti-PD-1 immunotherapy in melanoma patients. *Science* **359**, 97–103 (2018).
49. Li, Y. et al. Magnolol-driven microbiota modulation elicits changes in tryptophan metabolism resulting in reduced skatole formation in pigs. *J. Hazard Mater.* **467**, 133423 (2024).
50. Thiele Orberg, E. et al. Bacteria and bacteriophage consortia are associated with protective intestinal metabolites in patients receiving stem cell transplantation. *Nat. Cancer* **5**, 187–208 (2024).
51. Tang, T. W. H. et al. Loss of gut microbiota alters immune system composition and cripples postinfarction cardiac repair. *Circulation* **139**, 647–659 (2019).
52. Zhou, J. et al. Fecal microbiota transplantation in mice exerts a protective effect against doxorubicin-induced cardiac toxicity by regulating Nrf2-mediated cardiac mitochondrial fission and fusion. *Antioxid. Redox Signal.* **41**, 1–23 (2024).
53. Mamic, P. & Lanfear, D. E. Gut microbiome in cardiovascular disease and heart failure: seeing the iceberg below its surface. *JACC Heart Fail.* **11**, 822–824 (2023).
54. Pirozzi, C. et al. Palmitoylethanolamide counteracts high-fat diet-induced gut dysfunction by reprogramming microbiota composition and affecting tryptophan metabolism. *Front. Nutr.* **10**, 1143004 (2023).
55. Bender, M. J. et al. Dietary tryptophan metabolite released by intratumoral *Lactobacillus reuteri* facilitates immune checkpoint inhibitor treatment. *Cell* **186**, 1846–1862.e26 (2023).
56. Agus, A., Planchais, J. & Sokol, H. Gut microbiota regulation of tryptophan metabolism in health and disease. *Cell Host Microbe* **23**, 716–724 (2018).
57. Xue, H. et al. Gut microbially produced indole-3-propionic acid inhibits atherosclerosis by promoting reverse cholesterol transport and its deficiency is causally related to atherosclerotic cardiovascular disease. *Circ. Res.* **131**, 404–420 (2022).
58. Jia, D. et al. Microbial metabolite enhances immunotherapy efficacy by modulating T cell stemness in pan-cancer. *Cell.* **187**, 1651–1665.e21 (2024).
59. Zhang, D. et al. Kynurenine promotes neonatal heart regeneration by stimulating cardiomyocyte proliferation and cardiac angiogenesis. *Nat. Commun.* **13**, 6371 (2022).
60. Volkova, M., Palmeri, M., Russell, K. S. & Russell, R. R. Activation of the aryl hydrocarbon receptor by doxorubicin mediates cytoprotective effects in the heart. *Cardiovasc. Res.* **90**, 305–314 (2011).
61. Ghigo, A., Laffargue, M., Li, M. & Hirsch, E. PI3K and calcium signaling in cardiovascular disease. *Circ. Res.* **121**, 282–292 (2017).
62. Niborski, L. L. et al. CD8+T cell responsiveness to anti-PD-1 is epigenetically regulated by Suv39h1 in melanomas. *Nat. Commun.* **13**, 3739 (2022).
63. Li, G. et al. Gut microbiota aggravates neutrophil extracellular traps-induced pancreatic injury in hypertriglyceridemic pancreatitis. *Nat. Commun.* **14**, 6179 (2023).
64. Sun, J. et al. Microbiota-derived metabolite Indoles induced aryl hydrocarbon receptor activation and inhibited neuroinflammation in APP/PS1 mice. *Brain Behav. Immun.* **106**, 76–88 (2022).
65. Ma, Z.-G. et al. IIRX2 regulates angiotensin II-induced cardiac fibrosis by transcriptionally activating EGR1 in male mice. *Nat. Commun.* **14**, 4967 (2023).
66. Ma, Z.-G. et al. Toll-like receptor 5 deficiency diminishes doxorubicin-induced acute cardiotoxicity in mice. *Theranostics* **10**, 11013–11025 (2020).
67. Gesper, M. et al. Gut-derived metabolite indole-3-propionic acid modulates mitochondrial function in cardiomyocytes and alters cardiac function. *Front. Med.* **8**, 648259 (2021).
68. Horikawa, Y. T. et al. Cardiac-specific overexpression of caveolin-3 attenuates cardiac hypertrophy and increases natriuretic peptide expression and signaling. *J. Am. Coll. Cardiol.* **57**, 2273–2283 (2011).
69. Ma, Z.-G. et al. C1q-tumour necrosis factor-related protein-3 exacerbates cardiac hypertrophy in mice. *Cardiovasc. Res.* **115**, 1067–1077 (2019).
70. Wu, Q. et al. Dapagliflozin protects against chronic heart failure in mice by inhibiting macrophage-mediated inflammation, independent of SGLT2. *Cell Rep. Med.* **4**, 101334 (2023).

Acknowledgements

This work is supported by grants from the Fundamental Research Funds for the Central Universities (2042024YXA004), the National Natural Science Foundation of China (No. 82070410, 82270248), The Young Top-notch Talent Cultivation Program of Hubei Province, Knowledge Innovation Program of Wuhan-Basic Research.

Author contributions

Rong Huang, Zhuo-Yu Shen, Qi-Zhu Tang, and Zhen-Guo Ma conceived the project, designed the experiments, and planned the research. Rong Huang, Zhuo-Yu Shen, Dan Huang, and Shu-Hong Zhao performed most of the experiments. Ling-Xuan Dan and Pan Wu performed part of the experiments. Rong Huang, Zhuo-Yu Shen, and Zhen-Guo Ma collected the data and analyzed. Dan Huang, Shu-Hong Zhao, and Pan Wu provided technical support. Rong Huang, Zhuo-Yu Shen, Qi-Zhu Tang, and Zhen-Guo Ma drafted the paper. Dan Huang, Shu-Hong Zhao, and Qi-Zhu Tang edited the manuscript. All authors' feedback and convinced the final version for submission.

Competing interests

The authors declare no competing interests.

Additional information

Supplementary information The online version contains supplementary material available at <https://doi.org/10.1038/s41467-025-58107-8>.

Correspondence and requests for materials should be addressed to Zhen-Guo Ma.

Peer review information *Nature Communications* thanks Nicola Maurea, and the other, anonymous, reviewer(s) for their contribution to the peer review of this work. A peer review file is available.

Reprints and permissions information is available at <http://www.nature.com/reprints>

Publisher's note Springer Nature remains neutral with regard to jurisdictional claims in published maps and institutional affiliations.

Open Access This article is licensed under a Creative Commons Attribution-NonCommercial-NoDerivatives 4.0 International License, which permits any non-commercial use, sharing, distribution and reproduction in any medium or format, as long as you give appropriate credit to the original author(s) and the source, provide a link to the Creative Commons licence, and indicate if you modified the licensed material. You do not have permission under this licence to share adapted material derived from this article or parts of it. The images or other third party material in this article are included in the article's Creative Commons licence, unless indicated otherwise in a credit line to the material. If material is not included in the article's Creative Commons licence and your intended use is not permitted by statutory regulation or exceeds the permitted use, you will need to obtain permission directly from the copyright holder. To view a copy of this licence, visit <http://creativecommons.org/licenses/by-nc-nd/4.0/>.

© The Author(s) 2025